Inverse energy cascade and turbulent transport in a quasi-two-dimensional magnetized electrolyte system: An experimental study

L. Bardóczi
Budapest University of Technology and Economics, Budapest, Hungary

M. Berta
Széchenyi István University, EURATOM Association, Győr, Hungary

A. Bencze
Wigner RCP, RMKI, and EURATOM Association, Budapest, Hungary

(Received 27 May 2011; revised manuscript received 4 October 2011; published 30 May 2012)

We present an experimental study of the inverse energy cascade, spectral condensation, and turbulent particle transport in an electromagnetically driven thin layer of NaCl electrolyte. The presence of the bottom friction provides an energy sink at large scales for the turbulent flow. This energy sink crucially contributes to the balance of the forcing and dissipation which makes the inverse cascade steady. The present work provides an estimation of the linear dissipation rate on an experimental basis. We also show how the dissipation rate affects the characteristic features of the velocity spectrum and the dynamics of the spectral condensation. A quantitative study of the turbulent diffusion shows a significant decrease of the radial transport during the spectral condensation process.

DOI: 10.1103/PhysRevE.85.056315 PACS number(s): 47.27.De

I. INTRODUCTION

The concept of an inverse energy cascade originates from the famous groundwork of Kraichnan [1] who first proposed that energy and enstrophy can cascade in two dimensions. This dual cascade was found to be the consequence of the presence of two quadratic invariants: the mean-squared velocity and the mean-squared vorticity. The Kraichnan phenomenology predicts for the inverse cascade a self-similar range of scales with energy spectrum scaling as $E(k) \propto k^{-5/3}$. In Kraichnan's view, the inverse energy cascade cannot be stationary in a pure two-dimensional (2D) system, and a sink of energy at large scales is required to reach a stationary state; moreover, Kraichnan also conjectured that in finite systems the energy will condense in the lowest accessible k mode. This implies that the inverse cascade can be considered as a transient state which evolves towards the condensed state. Since then, this conjecture got strong support from both computer simulations [2] and laboratory experiments [3,4].

It was first mentioned by Shats and Punzmann [5] that besides the fundamental scientific importance of understanding the spectral condensation dynamics in 2D turbulence, it may have practical impact, e.g., in the field of magnetically confined fusion, namely, the understanding of the low-to-high (L-H) confinement transition and the appearance of coherent mesoscopic flows (zonal flows) [6–9]. From this point of view the change in the turbulent transport in the presence of large-scale coherent flows is a crucial issue [10].

In the present paper we focus on two aspects of the condensation process: first the dynamics of the transition from disordered turbulent flow to ordered coherent global flow is considered, and second a quantitative description is proposed for the turbulent transport in the presence of large-scale flow. One of the main control parameters which determines the final state of such laboratory systems as our quasi-2D magnetized electrolyte is the linear friction imposed by the rigid bottom wall of the container. The central role of this linear dissipation in the development of spectral characteristics of the direct enstrophy cascade has been recently demonstrated by Boffetta and co-workers, showing a systematic departure from Kraichnan's $E(k) \propto k^{-3}$ prediction [11]. We study here the counterpart of Boffetta *et al.*'s experiments, namely, the effect of the bottom friction on the energy spectrum in the inverse energy cascade range as well as on the spectral condensation regime.

Recently Shats and co-workers [12] have conducted a similar experiment to clarify the role of three-dimensionality in such thin magnetized electrolyte layers. They found that the relative importance of the z component of the velocity scales linearly with the normalized electrolyte depth. As three-dimensionality increases, the induced 3D turbulent motions make the turbulent viscosity stronger, resulting in the inhibition of spectral condensation. Since the electromagnetic forcing directly introduces 3D motions, we show in the present experiment that this effect can be avoided using weaker forcing for thicker layers.

II. EXPERIMENTS

A. Experimental setup

Forced quasi-two-dimensional turbulence has been studied experimentally in thin layers (3–8 mm) of NaCl electrolyte in a static electromagnetic field. The experimental setup is similar to the ones already presented in the literature [4,13] and the sketch is shown in Fig. 1(a). The electrolyte is placed in a plastic container of $12 \times 12 \times 2$ cm^3. A spatially periodic magnetic field is generated by 5×5 cylindrical neodymium magnets that are placed horizontally below the container with alternating poles (the maximum magnetic field is 0.3 T). The transverse dimension of the magnets is 0.5 cm, and the spacing between magnets is 1 cm, resulting in an injection wave

 ©2012 American Physical Society

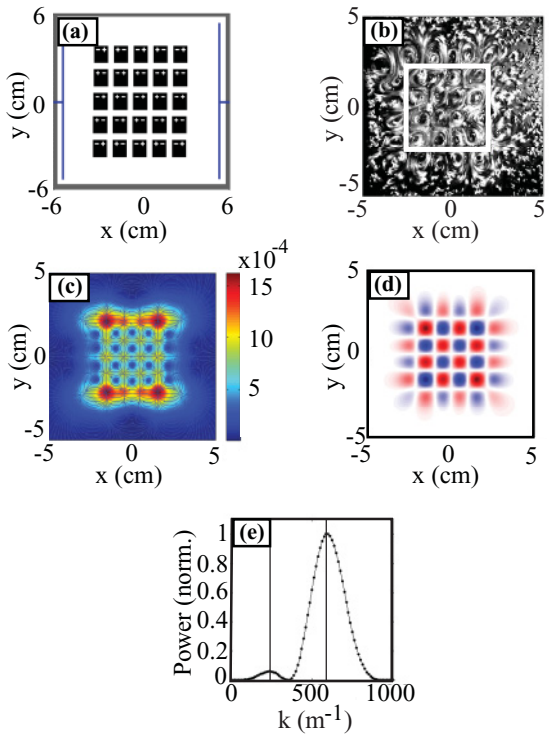

FIG. 1. (Color online) (a) Schematic view of the experimental setup, (b) initial state with 16 central vortices in a 3-mm-thick electrolyte layer, (c) numerically calculated magnetic field in T, (d) numerically calculated vorticity field, and (e) k spectrum of the numerically calculated vorticity field.

number (k_{inj}) of 628 m^{-1}. The electric field is generated by two electrodes immersed into the electrolyte at the edges of the container. The direction of the field is orthogonal to the magnetization axis of the magnets ($E = E_y = 1.6$ V/cm).

Observations have been made by a commercial digital camera placed above the experimental device. This camera records a video stream with a spatial resolution of 640 × 480 pixels at a rate of 30 frames per second. From the geometrical and optical constraints, the spatial resolution at the image plane is 0.25 mm/pixel.

Figure 1(b) shows a typical initial configuration of the flow 1 s after the onset of the electric current. The frame presented is averaged over 1 s of the flow evolution. As can be seen, 4 × 4 counter-rotating vortices are generated in the central part of the tank. This array of 16 vortices is bounded by a series of weaker counter-rotating vortices.

It can be shown that the vorticity field in an electromagnetically driven system at $t = 0$ is proportional to $[\nabla \times (\mathbf{E} \times \mathbf{B})]_z$. This fact gives us the possibility to design the initial vorticity configuration of our system by numerically calculating the magnetic field and keeping the electrostatic field homogeneous. Following the temporal evolution of the flow from different exotic initial vorticity fields, such as, e.g., dipole or quadrupole vortex lattices, we can study the interaction of coherent structures in turbulent media. This will be the subject of a subsequent presentation. Here we just describe in some detail the field calculation process.

In Figs. 1(c)–1(e) we show the results of a numerical calculation of the magnetic field based on the numerical integration of the Biot-Savart law provided that the permanent magnets can be replaced by solenoids with identical geometry. The numerical scheme has been tested in analytically well-known geometries (e.g., straight conductors, conducting loops, single solenoids, etc.), and it was found that Maxwell's equations are satisfied within a 10^{-7} relative error. Knowing the electric and the magnetic fields, $[\nabla \times (\mathbf{E} \times \mathbf{B})]_z$ can be determined [see Fig. 1(d)].

According to the k spectrum of this theoretically expected vorticity field [see Fig. 1(e)], the injection wave number appears to be 628 m^{-1}, which is consistent with the k value determined by the distance between the magnets. Interestingly, a local maximum appears at $k_{\mathrm{inj}} = 236$ m^{-}1 due to the finite number of magnets [see Figs. 1(c) and 1(e)]. Before discussing the experimental results, we briefly describe the measurement techniques used to obtain the temporal evolution of the random velocity field.

B. Overview of experiments

Experiments were done with different thicknesses (h) of the electrolyte layer; this allows us to control the linear dissipation rate. A constant electric current of 1 A was driven through the system while all parameters were kept constant.

In order to keep the dissipation rate at reasonably low levels and at the same time assure the quasi-two-dimensionality of the flow, the electrolyte layer depth was chosen between 3 and 8 mm.

As the electric current was kept constant, the current density scales as $j \sim 1/h$; this allows the forcing to be adjusted in such a way that the externally induced 3D turbulent viscosity remains weak and the inverse energy cascade can take place.

The length of the measurements was 1 min. This was limited by the dissolving metals of the electrodes, which cause the undesirable growth of viscosity and density in the thin-layer experiments at 1 A current. This effect can be identified by the slow decay of the total kinetic energy during the stationary regime.

To sum up the experimental circumstances, the following parameters were varied by varying the thickness: (1) the dissipation rate (2) the forcing, and (3) the two-dimensionality of the flow. All the other parameters were fixed.

C. Determination of the velocity field

The primary quantity in the present experiment is the time-evolving velocity field $\mathbf{v}(x,y,t)$. Other quantities of physical interest can be derived mathematically from $\mathbf{v}(x,y,t)$. The determination of the velocity field has been done using the particle image velocimetry (PIV) technique which is based on two-dimensional cross-correlation functions [14]. For visualization of the turbulent flow, uniformly distributed semolina grains were used as tracer particles with a typical size of 0.5 mm ≈ 2 pixels. Those particles which were sitting on the bottom of the container were carefully excluded from the data processing; therefore only the free surface motions were analyzed.

Each recorded movie frame is represented by a matrix $M_t(x,y)$. The $M_t(x,y)$ matrix covers the fluid domain determined by $[x,y] \in [-2.5,2.5] \times [-2.5,2.5]$. This matrix is divided into submatrices $S_{i,j,t}(x,y)$ and the two-dimensional

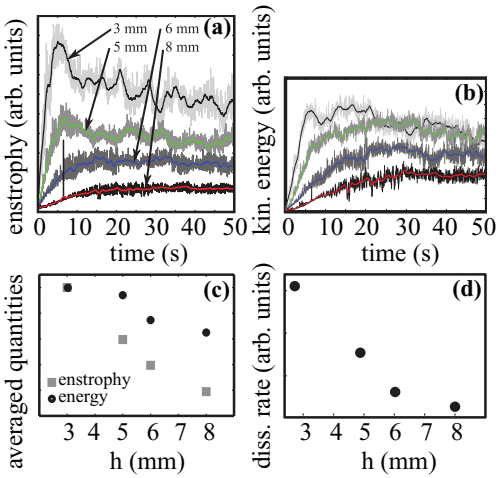

FIG. 2. (Color online) Time evolution of (a) enstrophy and (b) energy; (c) mean of total kinetic energy and enstrophy in the stationary regimes versus thickness (in relative units); (d) dissipation versus the thickness.

cross-correlation function is computed for the corresponding submatrices of consecutive frames. The displacement field is determined by the shift of the cross-correlation maximum with respect to zero spatial shift. By dividing the displacement field by the sampling time, one can get the velocity field. This method allows the calculation of the velocity field at 59×59 points with 30 Hz sampling frequency. The typical length of our experiments (1 min) allows us to measure the stationary regime for several tens of seconds. The total statistical uncertainty was estimated to be less than 10%, and originates from the uncertainty in the determination of time resolution and from the error caused by the PIV technique.

III. EXPERIMENTAL RESULTS

A. Time evolution of the energy and enstrophy

The total kinetic energy and enstrophy are defined by the following relations:

$$E(t) = \int \mathbf{v}^2(x,y,t)dxdy, \tag{1}$$

$$Z(t) = \int [\nabla \times \mathbf{v}(x,y,t)]^2 dxdy. \tag{2}$$

The evolution of enstrophy and total kinetic energy at different thicknesses can be seen in Figs. 2(a) and 2(b).

The plots show that at the beginning of each experiment the energy and the enstrophy grow linearly. Afterward, these quantities turn to stationarity. For the thinnest layer ($h =$ 3 mm) the total kinetic energy starts to decay after 25 s, which indicates the effect of the dissolving metals; therefore we processed only this time interval from the stationary regime. For thicker layers this problem can be neglected until 45 s; therefore we processed corresponding signals until 40 s. The mean of the total kinetic energy and enstrophy in the stationary regime show monotonic dependence on the layer thickness; see Fig. 2(c). The slopes of the linear parts of the curves also show monotonic dependence on the thickness and can be used to estimate the dissipation rate from the measurement.

In our description the friction due to the bottom wall is taken to be proportional to the magnitude of the flow velocity. From this model it is clear that at $t = 0$ the dissipation rate [$\varepsilon(t)$, the total dissipated energy per unit time] is zero. In a given experiment the electromagnetic forcing rate is $\partial_t j = \partial_t \dot{E}_{\text{in}} = 0$ (where $\dot{E}_{\text{in}}$ is the rate of the energy inflow). Therefore in the initial state the increment of the total kinetic energy ($\dot{E}_{\text{kin}}$) is determined only by the energy inflow [$\dot{E}_{\text{kin}}(t = 0) = \dot{E}_{\text{in}}$]. This means that the time dependence of the kinetic energy in the initial state is linear, as can be seen from the experiments [see Fig. 2(b)]. Moreover, taking the stationary state ($\dot{E}_{\text{kin}} = 0$) one can say that the energy inflow is balanced by the dissipation rate:

$$\varepsilon(\text{stationaryphase}) = \dot{E}_{\text{in}} = \dot{E}_{\text{kin}}(t = 0). \tag{3}$$

Therefore the dissipation rate in the stationary phase can be determined experimentally as the slope of the total kinetic energy in the initial phase.

Figure 2(d) shows that the dissipation rate decays as the thickness of the electrolyte increases.

B. Time evolution of vorticity fields

The vorticity field was numerically computed as the curl of the velocity field. The measured flow evolution shows three different phases. In the initial phase [$\sim$(0,7) s] structures with linearly growing energy [see Fig. 2(a)] are forced by the electromagnetic field. According to our observations one can speculate that above a critical velocity the initial vortices are destabilized and their energy is accumulated into lower wave numbers. This transient phase is called an inverse energy cascade [$\sim$(7,15) s]. As a result of this inverse energy cascade, in the stationary phase, a large stable vortex is formed (condensate) [$\sim$(15,50) s]; its size is comparable with the size of the flow. Figure 3 shows the vorticity field in the initial, transient, and stationary regimes at each thicknesses.

The measured vorticity in the initial state shows a reasonably good agreement with the numerical calculation presented in Fig. 1(d). This indicates that the forcing of the surface is dominated by the electromagnetic field.

In the next section we present a detailed description of the inverse energy cascade phase in terms of different spectral quantities.

C. Inverse energy cascade

In the x direction, one-dimensional k spectra of $v_x(x, y_i, t_j)$ were calculated at fixed y_i and t_j and then averaged along the y coordinate. As a result we got spectra computed from 59 points and 59 spectra were used for the averaging procedure. This was repeated for each t_j, resulting in the $E(k_x,t)$. The same procedure was done for $E(k_y,t)$. In order to decrease the statistical noise, a time average over 0.5 s was also performed.

The injection wave number appears to be 597 m^{-1} [see Fig. 4(a)]. This observation is consistent with the k spectrum of the forcing calculated on the base of the numerically calculated magnetic field [see Fig. 1(e)]. It is also clear that the energy content of spectral components at both injection wave numbers decreases with the increasing electrolyte thickness [see Figs. 4. and 5(a)]. It has to be mentioned that not only does the absolute value of the energy content decrease with increasing thickness,

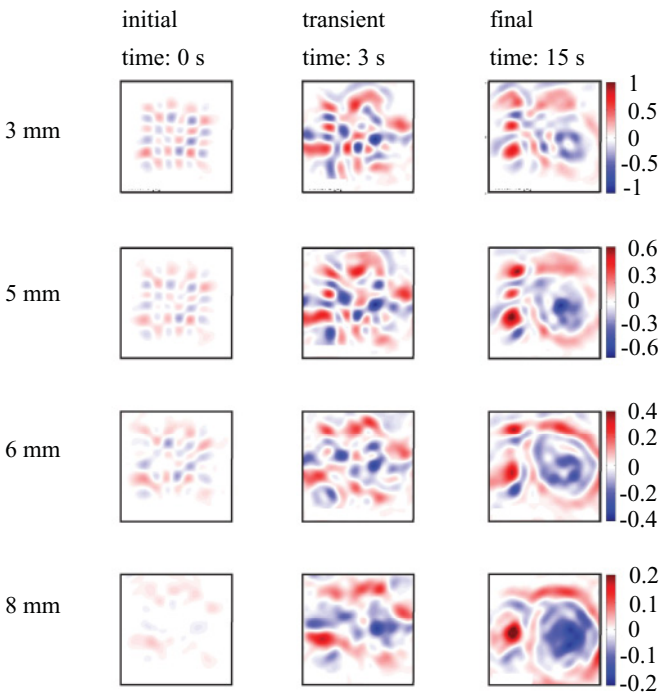

FIG. 3. (Color online) Evolution of vorticity fields. Columns: initial, transient, and stationary regimes. Rows: 3, 5, 6, and 8 mm thickness. Units are the same in each plot; color scales are adjusted to the maximum vorticity of the stationary states.

but also the ratio of the energy content of the two injection scales changes.

In the transient and stationary phases at $k = [200,500]$ m^{-1}, the energy spectra follow a power-law dependence, which is a signature of the presence of inertial range in the energy cascade. It is also important to note that the spectral exponent varies as the fluid thickness changes, which means that the presence of linear dissipation in a quasi-2D turbulent system greatly affects the spectral exponent [see Figs. 5(b) and 5(c)]. It was found that around 5 mm thickness the spectrum follows the $-5/3$ law and in the condensate state this power is around -3.23, which is in excellent agreement with the previous experiment [10], where it was found to be -3.3. The relative error of the spectral exponents has been estimated, and

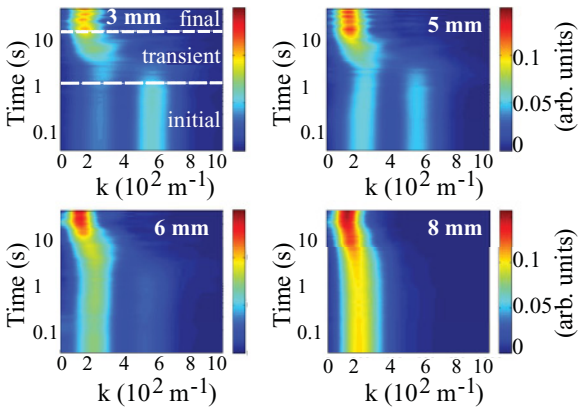

FIG. 4. (Color online) Time evolution of k spectra at 3, 5, 6, and 8 mm thicknesses.

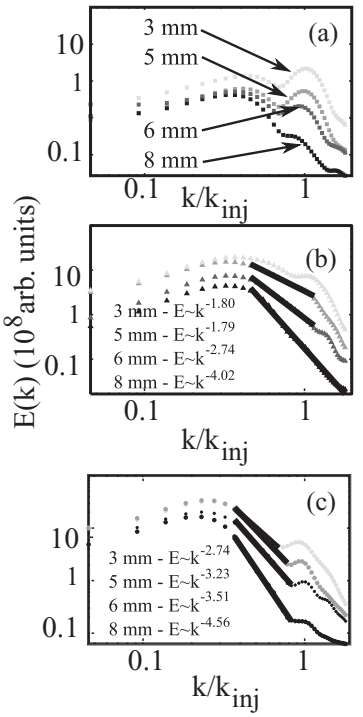

FIG. 5. Experimental k spectra of (a) initial, (b) transient, and (c) stationary regimes.

it was found to be less than 5% for the fitting procedure. If we consider the errors caused by the measurement technique and the data processing methods (10%), the total estimated average error of the spectral exponents is less than 12%. Data are listed in Table I and plotted on Fig. 6.

Another important rule has been established which describes the dynamics of the transition to the condensate state. The time evolution of the maximum energy in the k space [see Fig. 7(a)] was computed by fitting a parabola around the maximum. During the inverse energy cascade, the energy accumulation toward lower wave numbers is linear in log-log scale, described by the following rule:

$$k_{max} \propto t^{-\beta}. \quad (4)$$

The final average wave number (which is approximately the inverse average size of the condensate) and the duration of the spectral rearrangement versus the dissipation rate are plotted in Figs. 7(b) and 7(c). These plots show that with increasing fluid thickness (corresponding to decreasing dissipation) the duration of the condensation process also increases [see

TABLE I. Measured spectral exponents for different layer thicknesses in different states of the flow.

Transient state			Stationary state		
h (mm)	Spectral exponent	Rel. error (%)	h (mm)	Spectral exponent	Rel. error (%)
3	−1.38	13	3	−2.86	11
5	−1.73	11	5	−3.20	10
6	−2.42	11	6	−3.45	11
8	−4.12	10	8	−4.46	10

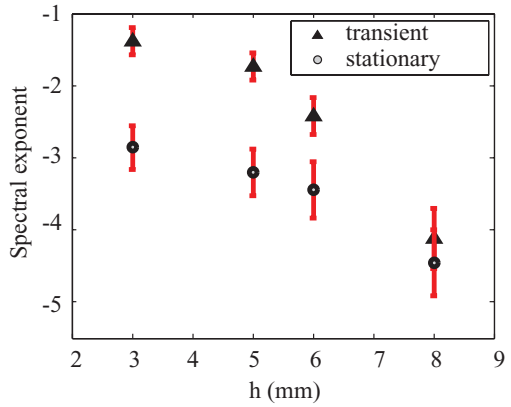

FIG. 6. (Color online) Measured spectral exponents as functions of thickness h.

Fig. 7(c)] and at the same time bigger structures build up [see Fig. 7(b)].

D. Particle motion

As the spectral energy is transferred to lower wave numbers, the appearance of condensates cause a significant decrease in the tracer particles' diffusion level and triggers ordered motion along the azimuthal coordinate. Although

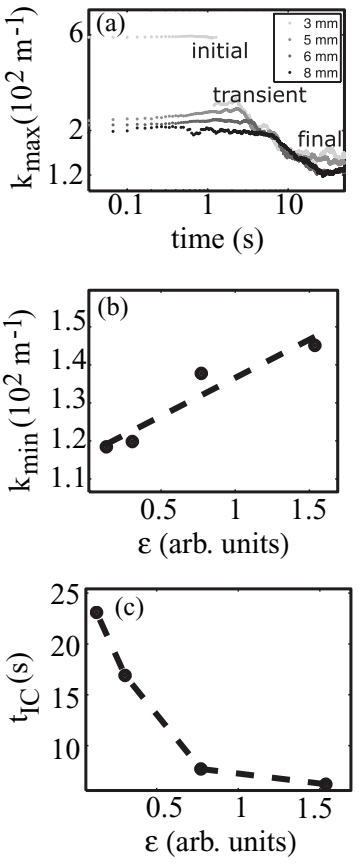

FIG. 7. (a) Time evolution of the most energetic wave number, (b) average of the most energetic wave number in the condensed state (inverse condensate size), and (c) duration of the spectral rearrangement versus dissipation.

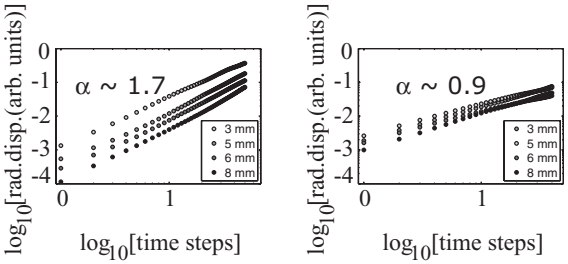

FIG. 8. Radial displacement (a) in the transient state and (b) in the final state.

some observations have been reported about the effect of condensates on radial particle transport [5,10,15], in this section we report a quantitative study to describe the effect of spectral condensation on particle transport, and this can also be considered as an independent experimental verification of the transport reduction using a different quantitative method through three transport parameters. The trajectories of about 2300 virtual particles were computed in the measured velocity fields by the following expression:

$$\mathbf{r}_i(t_j + \Delta t) = \mathbf{r}_i(t_j) + \mathbf{v}_i(\mathbf{r}_i(t_j), t_j)\Delta t, \tag{5}$$

where $\mathbf{r}_i(t)$ is the location of the ith particle at time t_j, and $\mathbf{v}_i(\mathbf{r}_i(t), t)$ is the velocity of this particle. The motion of tracers was followed for $T = n\Delta t$, where T was long enough for particles in the condensate state to get from one edge of the container to the other. All the parameters of this computation were fixed at each experiment.

The convective motion was measured with a high accuracy, while the diffusive motion of the particles is integrated over 4×4 mm^2 areas, defined by the size of the interrogation windows of the PIV method.

According to the theory of Brownian motion the average squared radial displacement of particles is $d(t) = \langle [r_i(t) - r_i(t = 0)]^2 \rangle_i \propto t^\alpha$. The motion is subdiffusive if $\alpha \leqslant 1$, diffusive if $\alpha = 1$, and superdiffusive if $\alpha \geqslant 1$ [16]. In the transient regime the value of the diffusion exponent α indicates superdiffusive radial transport; see Fig. 8(a). Since α drops from 1.7 to 0.9 in the stationary state, the radial transport becomes subdiffusive [see Fig. 8(b)]. We can also conclude that the diffusion exponent does not depend on the control parameter (h).

According to the parameter α, which globally characterizes turbulent transport in terms of diffusivity, two more specific quantities can be defined, in order to describe the particle transport in the azimuthal and radial directions:

$$L_m(t) = \frac{1}{N}\sum_{i=1}^{N} \max_{j,k}[|\mathbf{r}_i(t_j) - \mathbf{r}_i(t_k)|], \tag{6}$$

$$\sigma_{R(t)} = \frac{1}{N}\sum_{i=1}^{N} \sqrt{\sum_{j=1}^{n} [r_i(t_j) - \langle r_i(t)\rangle_t]^2}. \tag{7}$$

$\sigma_{R(t)}$ measures fluctuations around the most likely radial position, and $L_m(t)$ characterizes the dynamics of buildup of the ordered azimuthal motion of the fluid.

Figure 9 shows the clear effect of the condensation process in each experiment. During the inverse energy cascade the

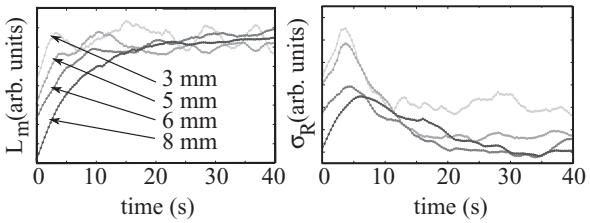

FIG. 9. (a) Averaged maximum displacement and (b) averaged variance of the radial coordinate.

variance of the radial coordinate [$\sigma_{R(t)}$, Fig. 9(b)] decreases to ≈60% of its maximum. Saturation of the length of the maximum displacement indicates that the particles make an ordered azimuthal motion around the center.

We can conclude that the formation of a condensate reduces the radial transport and orders the particle motion along the azimuthal coordinate.

IV. CONCLUSIONS

In the present work we have studied the formation of condensed quasi-2D flow placed in externally driven electromagnetic fields. We have concentrated our analysis on the changes of the spectral behavior and the particle transport.

From the spectral point of view we can conclude that the condensation process builds up larger structures in thicker layers where the dissipation rate is lower, and the transition time from the disordered state to the condensed state was found to be longer. During the spectral energy redistribution process, the most energetic wave number follows the power-law behavior $k_{\max} \approx t^{-\beta}$. The measured spectral exponents show monotonic dependence on the fluid thickness. Around 5 mm thickness we see a good agreement with the Kolmogorov turbulence theory and some previous experimental results [13,17].

A quantitative method has been developed for determination of the turbulent particle transport behavior in different states. The result of the analysis shows that the transport turns to subdiffusive in the stationary regime from the superdiffusive transport of the transient state. The condensation triggers ordered motion along the azimuthal coordinate and causes significant suppression of the radial particle transport (≈60%).

[1] R. H. Kraichnan, Phys. Fluids **10**, 1417 (1967).
[2] L. M. Smith and V. Yakhot, J. Fluid Mech. **274**, 115 (1994).
[3] J. Sommeria, J. Fluid Mech. **170**, 139 (1986).
[4] J. Paret and P. Tabeling, Phys. Fluids **10**, 3126 (1989).
[5] M. G. Shats, H. Xia, and H. Punzmann, Phys. Rev. E **71**, 046409 (2005).
[6] A. Bencze, M. Berta, S. Zoletnik, J. Stockel, J. Adamek, and M. Hron, Plasma Phys. Control. Fusion **48**, S137 (2006).
[7] P. H. Diamond, S-I. Itoh and T. S. Hahm, Plasma Phys. Control. Fusion **47**, R35 (2005).
[8] A. Fujisawa, Nucl. Fusion **49**, 013001, (2009).
[9] Andrew P. L. Newton and Eun-Jin Kim, Phys. Plasmas **18**, 052305 (2011).
[10] M. G. Shats, H. Xia, H. Punzmann, and G. Falkovich, Phys. Rev. Lett. **99**, 164502 (2007).
[11] G. Boffetta, A. Cenedese, S. Espa, and S. Musacchio, Europhys. Lett. **71**, 590 (2005).
[12] M. G. Shats, D. Byrne, and H. Xia, Phys. Rev. Lett. **105**, 264501 (2010).
[13] J. Paret and P. Tabeling, Phys. Rev. Lett. **79**, 4162 (1997).
[14] M. Raffel, Ch. E. Willert, S. T. Wereley, and J. Kompenhans, *Particle Image Velocimetry: A Practical Guide* (Springer, Berlin, 2007).
[15] M. G. Shats and H. Xia, Plasma Fusion Res. **4**, 012 (2009).
[16] R. Balescu, Phys. Rev. E **51**, 4807 (1995).
[17] J. Paret, M. C. Jullien, and P. Tabeling, Phys. Rev. Lett. **83**, 3418 (1999).